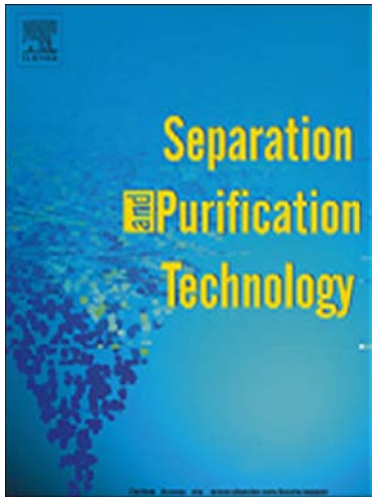

The effect of surfactants on the photocatalytic properties of the heterogeneous magnetic zinc oxides nanoparticles

Xiaohui Feng, Xia Lou

PII: S1383-5866(15)00269-5
DOI: http://dx.doi.org/10.1016/j.seppur.2015.04.036
Reference: SEPPUR 12318

To appear in: *Separation and Purification Technology*

Received Date: 23 February 2015
Revised Date: 17 April 2015
Accepted Date: 23 April 2015

Please cite this article as: X. Feng, X. Lou, The effect of surfactants on the photocatalytic properties of the heterogeneous magnetic zinc oxides nanoparticles, *Separation and Purification Technology* (2015), doi: http://dx.doi.org/10.1016/j.seppur.2015.04.036

The effect of surfactants on the photocatalytic properties of the heterogeneous magnetic zinc oxides nanoparticles

Xiaohui Feng, Xia Lou*

Department of Chemical Engineering, Curtin University, Kent Street, Bentley, WA 6102, Australia

*Corresponding author: Email: x.lou@curtin.edu.au; Tel.: +61 8 9266 1682; Fax: +618 9266 2681.

Abstract

The article reports the synthesis and characterization of two new magnetite (Fe_3O_4)-supported zinc oxide (ZnO) photocatalysts, produced in the presence of Fe_3O_4 nanotemplates that were bound with tetramethylammonium (TMAH) and citric acid (CA) respectively. The TMAH-bound hybrid nanoparticles, Fe_3O_4(TMAH)-ZnO, have demonstrated a high recoverability (86%) and phenol degradation rate constant of 0.0170 min^{-1}, which is much greater than that of the CA-bound photocatalyst (0.0085 min^{-1}) and the pure form of ZnO (0.0039 min^{-1}). Further investigation demonstrates that the presence of various surfactants on the surface of the magnetite nano-templates significantly affects the sizes and surface properties of the produced hybrid nanophotocatalysts, and subsequently their photocatalytic activities. The pH values of the photocatalysis environment also show strong influences to the photocatalytic properties and the dissolution of the nanoparticles. An optimal operation condition for the Fe_3O_4(TMAH)-ZnO is when the photocatalysis is carried out at a pH = 4~5.6, and the concentrations of the photocatalyst and phenol are 325 and 20 mg L^{-1}, respectively.

Keywords: magnetic photocatalysts; zinc oxide; photocatalysis; phenol degradation; surfactants bound iron oxide.

1. Introduction

There has always been a demand for cost effective, high performance, reusable/recoverable photocatalysts. Magnetic nanoparticles have been used to produce such catalysts, in which the catalytically active molecules are fabricated with a solid support of magnetic nanoparticles, and the resulted catalysts are classified as heterogeneous [1]. While the magnetic properties are used for effective separation and recovery of the catalysts, the large surface areas of the nanoparticles ensure high catalytic activities of the catalytically active molecules. Among various magnetic nanoparticles, magnetite (Fe_3O_4) nanoparticles have been the most widely used magnetic supporting materials for the fabrication of such heterogeneous catalysts, owing to their low cost, simple preparation method, low toxicity and biocompatibility [2, 3]. Immobilisation of catalytic fragments, such as metal oxides, has been proven to be very effective. A great deal of research work has been reported on the titanium dioxide-based magnetically separable photocatalyst (Fe_3O_4/TiO_2) which has shown great reusability [4]. Enhanced photocatalytic activity has been seen in various forms of magnetic composites, including nanoparticles [5, 6], nanorods and nanosheets [7, 8], when TiO_2 or zinc oxide (ZnO) are immobilised on the surface of Fe_3O_4, reportedly due to the decelerated electron–hole recombination in the presence of iron ions. A recent study by our group has shown that zinc oxide deposited on the surface of the Fe_3O_4 nanoparticles enhances the photocatalytic activities of the pure ZnO nanoparticles, and the improved photocatalytic properties were well maintained after three cycles of usage [9].

In many of the reported works, a critical problem has been the aggregation of Fe_3O_4 nanoparticles caused by their smaller size with a larger surface area-to-volume ratio, high surface energy and inherent magnetic dipolar force [10]. Coating Fe_3O_4 nanoparticles, prior to the immobilisation of other components, with various surfactants such as tetramethylammonium (TMAH) or citric acid (CA) has been reported for the improvement of dispersion [11]. The surfactants can be either absorbed or chemically attached to the surfaces of nanoparticles to generate a double-layer protection [12], through the ensuing steric forces between nanoparticles that are able to balance the magnetic dipolar forces and electrostatic forces [13, 14]. However, little is known how these surfactants would affect the ultimate performance of the nanocatalysts that are generated from the surfactants-bound magnetite.

This paper reports the successful fabrication of Fe_3O_4-supported ZnO nanophotocatalysts, in the presence of THMA- and CA-bound Fe_3O_4 nano-templates, and the investigation results of the photocatalytic activities of the resultant heterogeneous photocatalysts, in relation to the

type of surfactants used, the catalyst dosage, the initial concentration of a model photodegradation compound (phenol), and the pH value of the reaction mixture. The TMAH-bound hybrid nanoparticles, Fe_3O_4(TMAH)-ZnO, have shown excellent rate constants of 0.0082 min^{-1} and 0.0170 min^{-1} towards phenol degradation at pH levels of 5.6 and 4, respectively, which are highly comparable to/greater than the values of 0.0020 min^{-1} and 0.0152 min^{-1} when equal amounts of the commercially available titanium dioxide (TiO_2), P25, were used under the same experimental conditions. A high recoverability (86%) of the magnetite-supported nanophotocatalyst was found for Fe_3O_4(TMAH)-ZnO. The effect of the size and varying surface properties, attributable to the presence of the surfactants, upon the performance of the hybrid nanoparticles will be discussed.

2 Experimental

2.1 Materials

Ferrous chloride tetrahydrate ($FeCl_2$•$4H_2O$, 99.99%), ferric chloride hexahydrate ($FeCl_3$•$6H_2O$, 99.99%), hydrochloric acid concentrate (HCl, 0.1 mol L^{-1}), sodium hydroxide (NaOH, ≥97.0%), zinc acetate dehydrate ($Zn(Ac)_2.2H_2O$, Ac=CH_3COO, ≥98%), diethylene glycol (DEG, 99%), sodium chloride (NaCl, ≥99.5%), phenol (C_6H_5OH, ≥96.0%), phosphate buffered saline (PBS), citric acid ($C_6H_8O_7$, ≥98%), sodium citrate dihydrate ($C_6H_5O_7Na_3$•$2H_2O$, ≥99.0%), sodium carbonate (Na_2CO_3, ≥99.5%) and sodium bicarbonate ($NaHCO_3$, 99%) were purchased from Sigma-Aldrich. Tetramethylammonium hydroxide (TMAH, 25%) was supplied by Fluka. Degussa P25 (TiO_2 nanoparticulate material consisting of 75% anatase and 25% rutile) was purchased from Degussa.

2.2 Synthesis of Fe_3O_4(TMAH) and Fe_3O_4(CA) nanoparticles

To 20 ml deionised water (DW), $FeCl_3$•$6H_2O$ (3.24 g, 0.012 mol) and $FeCl_2$•$4H_2O$ (1.19 g, 0.006 mol) were added and constantly stirred under nitrogen protection. The obtained iron salt solution was then gradually added to NaOH solution (100 ml, 0.5 M) under mechanical stirring. After stirring for 1 h, the black precipitate was collected by applying an external magnetic field and then washed five times with DW (5×10 ml).

To produce the TMAH-suspended iron oxide (Fe_3O_4(TMAH)), the obtained Fe_3O_4 nanoparticles (0.4 g, 1.73 mmol) were suspended in TMAH solution (0.5 ml) and then further diluted using DW to a total volume of 4.0 ml. For the CA-suspended nanoparticles (Fe_3O_4(CA)), the same amount of magnetite nanoparticles was dispersed into an aqueous

citric acid solution (5 ml, 0.1 M) followed by ultrasonic vibration for 30 min. Both suspensions were maintained at 4 ^{o}C for further investigation.

2.3 Preparation of Fe_3O_4-ZnO hybrid nanoparticles

Fe_3O_4-ZnO hybrid nanoparticles were fabricated using a previously reported method [9]. Fe_3O_4(TMAH) and Fe_3O_4(CA) were utilised as seeds to produce Fe_3O_4(TMAH)-ZnO and Fe_3O_4(CA)-ZnO, respectively. In brief, Fe_3O_4(TMAH) nanoparticles (0.2 g, 8.6 mmol) were suspended in 30 ml DEG, using ultrasonic vibration for 30 min, to form a homogeneous suspension. $Zn(Ac)_2$•$2H_2O$ (2.19 g, 0.01 mol) was added into DEG (100 ml) and the reaction mixture was heated to 150 ^{o}C with constant stirring under nitrogen protection. Then, the Fe_3O_4(TMAH) suspension was added, dropwise, followed by heating to 160 ^{o}C. After 2 h of reaction time, the reaction mixture was air cooled to room temperature. The resultant hybrid nanoparticles were collected by applying an external magnetic field. The obtained sample was washed five times with DW (5×15 ml) then three times with ethanol (3×15 ml) and dried under vacuum. A similar experiment was carried out using Fe_3O_4(CA) nanoparticles as seeds. The obtained hybrid nanoparticles were denoted as Fe_3O_4(TMAH)-ZnO and Fe_3O_4(CA)-ZnO. The reaction yields for Fe_3O_4(TMAH)-ZnO and Fe_3O_4(CA)-ZnO were 59.4% and 40.6%, respectively.

2.4 Size and size distribution of the obtained nanoparticles

A transmission electron microscope (TEM, JEOL JSM 2011) equipped with a Gatan Digital Camera was used to examine the morphology of all produced nanoparticles. Prior to the TEM examination, the sample was suspended in DEG by ultrasonication for 10 min, resulting in a final concentration of around 0.02 mg L^{-1}. Then one drop of the suspension was placed onto a copper grid (with a carbon film substrate) and the grid was dried in an oven at 100 ^{o}C, overnight. The TEM images were recorded at an accelerating voltage of 200 kV. The sizes of the nanoparticles were measured using the in-built JEOL operational software, DigtalMicrograph [15].

The particle sizes in both the aqueous solution and the DEG suspension were further estimated by dynamic light scattering (DLS) using a Malvern Zetasizer Nano-ZS. Prior to DLS analysis, samples were suspended in DW and DEG, respectively, using ultrasonic vibration. The suspensions were equilibrated to 20 ^{o}C. Each sample was measured in triplicate and the results were presented as mean ± standard deviation. The zeta potential also was

measured using the same equipment. Sodium chloride aqueous solution (10 ml, 0.01 mol L^{-1}) was used as a conductive regulator. The pH of the NaCl solution was adjusted to 4, 7, 8 and 10 by using an aqueous solution of NaOH (0.01 mol L^{-1}) and HCl (0.01 mol L^{-1}). The sample (1 mg) was suspended in each of the resulting solutions (10 ml) and allowed 20 min ultrasonic vibration prior to measurement. Three measurements were taken for each sample.

2.5 FTIR, UV-Vis and photoluminescence spectroscopic analysis

Fourier transform-infrared (FTIR) analysis was carried out using a Thermo Scientific Nicolet iS50 equipped with an Automated Beamsplitter Exchanger (ABX) having a resolution of 4 cm^{-1}. All the spectra were recorded from 200 to 4000 cm^{-1}. UV-visible diffuse reflectance spectra (UV-vis DRS) were collected on a Jasco V670 spectrophotometer with a Φ60 mm integrating sphere, using $BaSO_4$ as the reference material. UV-Vis DRS was monitored over a wavelength range of 300 nm to 700 nm, with a band width of 2 nm. The photoluminescence (PL) spectra of the samples were obtained using a Cary Eclipse (MY13060002) Fluorescence Spectrometer with an excitation wavelength of 390 nm. The emission spectra were recorded in the region of 370-410 nm and both excitation and emission slit widths were 5 nm. For sample preparation, the samples (around 10 mg) were suspended in deionised water and further diluted to 2 $\mu g\ ml^{-1}$.

2.6 ICP-AES and BET analysis

An inductively coupled plasma-atomic emission spectroscopy (ICP-AES) analysis was carried out to determine the ratio of iron and zinc elements in the hybrid nanoparticles, using a Vista Axial CCD Simultaneous ICP-AES Instrument. Brunauer-Emmett-Teller (BET) analysis was performed to evaluate the surface area, pore volume and pore size distribution of the hybrid nanoparticles, using nitrogen sorption at -196 ^{o}C on a Micromeritics Tristar 3000 apparatus. Prior to BET examination, samples were preheated to 200 ^{o}C under vacuum, overnight.

Table 1. Chemical and physical properties of the synthesized nanoparticles.

Sample ID	Fe_3O_4:ZnO	Particle size (nm)			Iron concentration* (mg L^{-1})	Pore size (nm)	Pore Volume (cm^3 g^{-1})	SurfaceArea (m^2 g^{-1})
		Dry	in DW	in DEG				
Fe_3O_4	1:0	10.6 ± 1.4	233.2 ± 1.2	57.3 ± 1.7	<dl	-	-	-
Fe_3O_4(CA)	1:0	7.1 ± 2.3	138.8 ± 1.2	17.5 ± 0.2	28.4	-	-	-
Fe_3O_4(TMAH)	1:0	10.5 ± 2	82.3 ± 5.7	8.3 ± 0.4	<dl	-	-	-
Fe_3O_4(TMAH)-ZnO	1:4.2	34.5 ± 6.2	-	-	-	5.8	0.19	95.6
Fe_3O_4(CA)-ZnO	1:1.6	293 ± 32	-	-	-	2	0.16	73.8
TiO_2	-	24 ± 1	-	-	-	2.1	0.21	68.9

* The iron concentrations were determined by ICP-AES for which the detection limit (dl) was 0.002 mg L^{-1}. DW was used as the sample matrix for the reported data.

2.7 Photoreactivity study

The photocatalytic performance of the magnetic ZnO hybrid nanoparticles was evaluated based on the phenol degradation rate constant under the irradiation induced by an MSR 575/2 metal halide lamp (575 W, Philips) with a wavelength ranging from 315 nm to 1050 nm, using a 1L double-jacketed reactor that was kept at 25±1 ^{o}C. During the experiment, a certain amount of the hybrid nanoparticles was suspended in aqueous phenol solution (200 ml) and was stirred at 600 rpm for 30 min, prior to exposure to the light. During the irradiation period, 10 ml of the suspension was withdrawn at each of the prescribed time intervals and filtered using a 0.45 μm Millipore filter to remove the residual hybrid nanoparticles. Each fraction of the liquid was analysed using an HPLC (Varian) to determine the phenol degradation rate. ICP-AES analysis was carried out on some of the samples to determine the iron and zinc elemental content in the solution. The full experimental details can be found in our previous work [16].

Various concentrations of the nanocatalysts and the initial phenol, as well as various pH values, were investigated using the above experimental procedure. Details are summarised in Table 2. Commercial TiO_2 (Degussa P25) also was investigated as a reference material. The buffer solutions of citric acid-sodium citrate, PBS and sodium carbonate-sodium bicarbonate were used to adjust the pH values of the phenol degradation mixtures, prior to the photocatalysis experiments.

Table 2. Kinetic parameters, phenol removal, and the dissolved content of iron and zinc, obtained using various reaction parameters.

Sample ID	Concentration ($mg\ L^{-1}$)			pH	Phenol removal (%)	Rate constant (k, min^{-1})	R^2	Iron Concentration* ($mg\ L^{-1}$)
	Catalysts	ZnO or TiO_2	Phenol					
ZnO	325	325	20	5.6	51.8	0.0039	0.997	n.a.
Fe_3O_4(TMAH)-ZnO	100	81	20	5.6	62.7	0.0062	0.989	<dl
	325	262	10	5.6	78.0	0.0099	0.994	<dl
	325	262	80	5.6	25.9	0.0022	0.938	<dl
	500	404	20	5.6	63.6	0.0067	0.991	<dl
	1000	808	20	5.6	57.5	0.0061	0.979	0.04
	325	262	20	2.5	51.9	0.0050	0.951	24
				4	100.0	0.0170	0.913	22
				5.6	71.3	0.0082	0.999	0.13
				8	30.8	0.0030	0.848	<dl
				10	14.5	0.0013	0.972	<dl
Fe_3O_4(CA)-ZnO	325	200	20	2.5	34.7	0.0041	0.988	28
				4	64.3	0.0085	0.987	26
				5.6	54.7	0.0045	0.971	0.06
				8	23.2	0.0023	0.999	0.05
				10	13.9	0.0013	0.981	0.03
TiO_2	325	325	20	4	16.3	0.0020	0.907	n.a.
	260	250	20	5.6	100	0.0152	0.960	n.a.
	325	325	20	5.6	100	0.0242	0.973	n.a.
	325	325	20	10	25.2	0.0025	0.960	n.a.

* The ion concentrations were determined by ICP-AES, for which the detection limit (dl) was 0.01 $mg\ L^{-1}$. Phenol solution was used as the sample matrix for the reported data.

3 Results and Discussion

3.1 Characterisation of Fe_3O_4, Fe_3O_4(TMAH) and Fe_3O_4(CA)

Fe_3O_4 nanoparticles obtained from this work were spherical-like, with an average size of 10.6±1.4 nm, and they tended to aggregate (Fig. 1a). The nanoparticles suspended in TMAH and CA, Fe_3O_4(CA) and Fe_3O_4(TMAH), appeared similar in geometry, but were apparently more uniform and spread further apart from each other (Fig. 1b-c). The average sizes of the nanoparticles were 7.1±2.3 nm and 10.5±2 nm for Fe_3O_4(CA) and Fe_3O_4(TMAH), respectively. The decreased particle size of Fe_3O_4(CA) is likely to be due to the formation of an iron complex with the citric acid that is leachable from the surfaces of solid particles to the aqueous acid solution [17]. The ICP-AES analysis demonstrated that there was 28.4 mg L^{-1} of elemental iron in the liquid obtained from the Fe_3O_4(CA) suspension, indicating 0.48% loss of the Fe_3O_4 into the citric acid solution. However, the Fe_3O_4 nanoparticles stored in deionised water and aqueous TMAH solution were stable, showing that iron ions in the tested solutions were below the detection limit of 0.002 mg L^{-1} (Table 1). The chemical dissolution of iron ions can be illustrated by the chemical reaction Eq. (1).

$$3Fe_3O_4 + 8R(COOH)_3 \Rightarrow 3Fe^{2+} + 6Fe^{3+} + 8R(COO^-)_3 + 12H_2O \quad (1)$$

The particle sizes and size distribution measured by the DLS are displayed in Fig. 1. Pure Fe_3O_4 nanoparticles suspended in deionised water showed an average hydrodynamic diameter of 233.2±1.2 nm, with a polydispersity index (PDI) of 0.262. This size was reduced to 138.8±1.2 nm for Fe_3O_4(CA) and 82.3±5.7 nm for Fe_3O_4(TMAH) after stabilising with the surfactants CA and TMAH, respectively. The significant decreases in the hydrodynamic diameters of Fe_3O_4(CA) and Fe_3O_4(TMAH) are an indication of the improved dispersity by the surfactants. In the presence of these surfactant molecules, the magnetic attraction force between the Fe_3O_4 nanoparticles is compensated by the electrostatic interparticle repulsion force [18]. Interestingly, when DEG was used as the suspension medium, the hydrodynamic diameters of the particles were further reduced to 57.3±1.7 nm, 17.5±0.2 nm and 8.3±0.4 nm for Fe_3O_4, Fe_3O_4(CA) and Fe_3O_4(TMAH), respectively, indicating that DEG also served as a good surfactant. DEG was used as a solvent for the fabrication of the designed heterogeneous photocatalysts, Fe_3O_4-ZnO, in this study. It should be noted that the hydrodynamic size of the nanoparticles is much larger than that obtained from TEM images, which is not uncommon. Particle aggregation and hydrodynamic influence are the main causes of this difference.

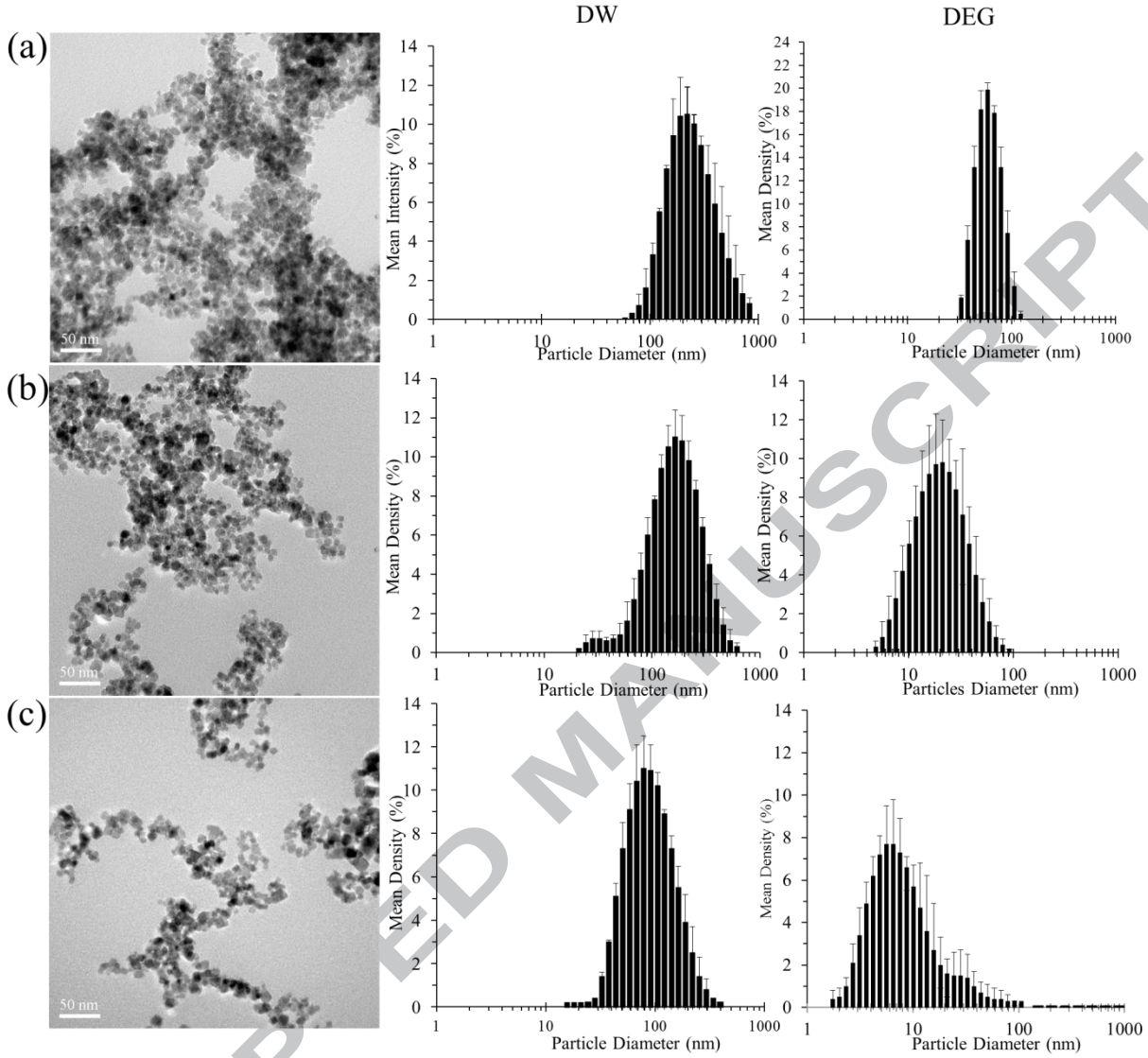

Fig. 1. TEM images and the corresponding DLS spectra of (a) pure Fe_3O_4, (b) Fe_3O_4(CA) and (c) Fe_3O_4(TMAH).

The measured zeta potentials of Fe_3O_4, Fe_3O_4(CA) and Fe_3O_4(TMAH) at various pH values are shown in Fig. 2. A decrease in the magnitude of zeta potential was demonstrated for all nanoparticles as the pH value increased from 4 to 10. For Fe_3O_4(TMAH), a drastic decrease from +52.5 mV to -55.4 mV was observed, showing an isoelectric point of pI=7.8. The high and positive value of the zeta potential of Fe_3O_4(TMAH) at pH<7.8 suggests that the $N(CH_3)_4^+$ ions from TMAH had accumulated on the surface of the nanoparticles, forming a positively charged shell. For pure Fe_3O_4, the zeta potential was negative over the investigated pH range, indicating the accumulation of –OH groups on the surface of the nanoparticles. For Fe_3O_4(CA), the change of zeta potential, as the pH value was changed, was similar to that of pure Fe_3O_4, being negative over the investigated pH range. The slightly more negative charge

of the shell in the former is probably due to the presence of citrate ions ($C_6H_5O_7^{3-}$). Under acidic conditions (pH<7), the zeta potential value increases with decreasing pH for Fe_3O_4(TMAH). However, it decreases with reduced pH values for both pure Fe_3O_4 and Fe_3O_4(CA). This would result in greater tendency for aggregation of Fe_3O_4 and Fe_3O_4(CA) under acidic conditions. Indeed, in both deionised water and DEG suspensions (pH~5-6), the sizes of these particles show a similar pattern of Fe_3O_4 > Fe_3O_4(CA) > Fe_3O_4(TMAH) (Fig. 1).

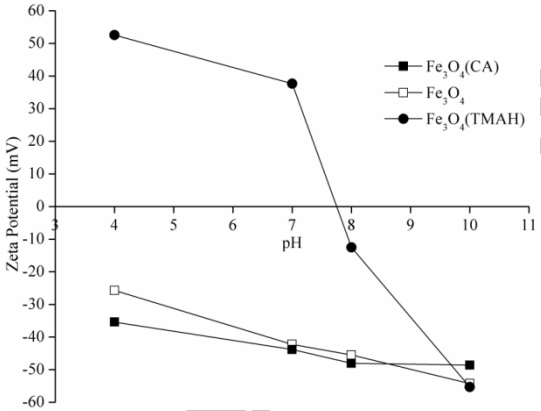

Fig. 2. Zeta potential value of various nanoparticles versus pH values.

The binding of $N(CH_3)_4^+$, or $(C_6H_5O_7)^{3-}$, or –OH on the surfaces of the Fe_3O_4 nanoparticles was further demonstrated by FTIR spectroscopy, as shown in Fig. 3. For pure Fe_3O_4 nanoparticles, the characteristic peak of the Fe-O bond in Fe_3O_4 nanoparticles appears at 530 cm^{-1}. There is a weak peak at 1640 cm^{-1} assignable to the bending vibration of –OH groups [19]. After citric acid was added, a new absorption peak appeared at 1560 cm^{-1}, which can be attributed to the symmetric stretching vibration of C=O from carboxylate (citrate ions). For pure citric acid, the absorption peak for C=O stretching vibration is at 1710 cm^{-1} [11]. The shift of the absorption peak to a lower wavenumber was a result of the formation of iron-citrate ion complex [20]. The absorption peak at 1380 cm^{-1} is due to the bond formed between iron and the carboxyl groups, and the weak band at 830 cm^{-1} was caused by the hydrogen bond between the carboxyl groups [21]. The overall results, through the chemisorption of the carboxylate groups by the Fe_3O_4, have yielded a negatively charged surface of the nanoparticles, as discussed in the previous section [22]. For Fe_3O_4(TMAH), the presence of tetramethylammonium cations was confirmed through the strong absorption peaks at 1490 cm^{-1} and 950 cm^{-1}, which are attributable to the asymmetric bending vibrations of $–CH_3$ groups and the asymmetric stretching vibrations of C-N groups, respectively. The

results further demonstrated that, in the TMAH-binded Fe_3O_4, $N(CH_3)_4^+$ ions were dissociated from the TMAH molecules and coupled with negatively charged Fe-OH bonds, forming a more stable, positively charged shell around the magnetite nanoparticles [23]. The electrochemical interreactions between Fe_3O_4 and the surfactants that were used are schematically displayed in Fig. 4.

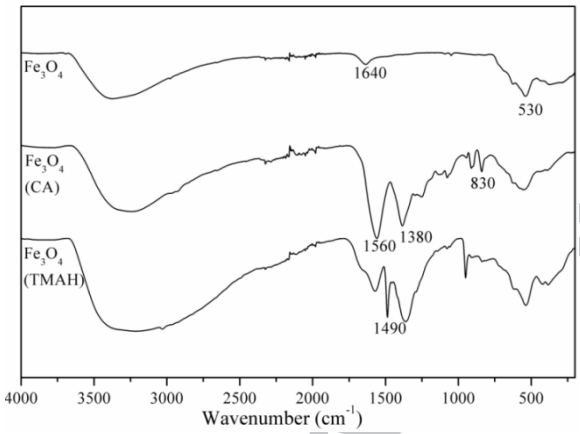

Fig. 3. FTIR spectra of Fe_3O_4, Fe_3O_4(CA) and Fe_3O_4(TMAH).

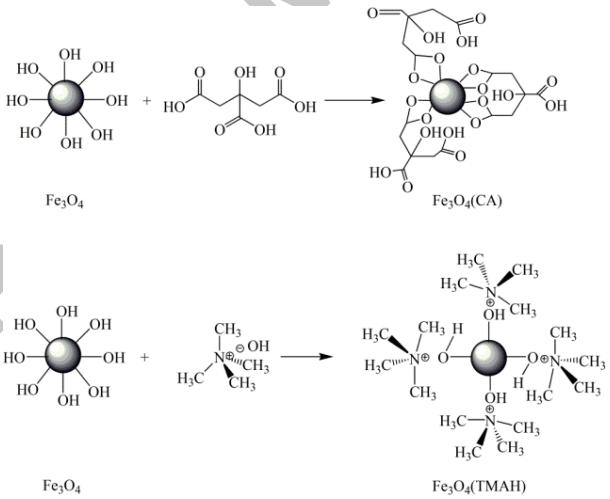

Fig. 4. Illustration of the electrochemical interreactions between Fe_3O_4 and the surfactants [23, 24].

3.2 Characterisation of Fe_3O_4(TMAH)-ZnO and Fe_3O_4(CA)-ZnO hybrid nanoparticles

The binding of the two different surfactants not only resulted in various surface and morphological properties of the Fe_3O_4 seeds, but also significantly affected the further formation of the heterogeneous hybrid nanophotocatalysts. TEM images, displayed in Fig. 5, show that the average size of Fe_3O_4(TMAH)-ZnO is 34.5±6.2 nm, while the Fe_3O_4(CA)-ZnO nanoparticles are 293±32 nm. The morphology also varies between the two; the former is

much denser while the latter appears to be looser. It should be noted that the condensation of $Zn(Ac)_2$ releases acetic acid (HAc), which is acidic. In this condition, Fe_3O_4(TMAH) nanoparticles are positively charged, as indicated by their zeta potential values. The positively charged Fe_3O_4(TMAH) nanoparticles are attractive to the negatively charged $[Zn(OH)_4]^{2-}$ species, leading to the deposition of ZnO on the surface of Fe_3O_4 nanoparticles, thereby forming a relatively dense morphology, as shown in Fig. 5a. The high zeta-potential value of Fe_3O_4(TMAH) has apparently resulted in a stronger attraction force between the two, leading to the formation of smaller sizes of the hybrid nanoparticles. On the other hand, the condensation of $Zn(Ac)_2$ on the surfaces of Fe_3O_4(CA) nanoparticles could be eliminated, due to the negatively charged CA, resulting in the loosely-formed structure of the ZnO layer, as demonstrated in Fig. 5b. The pure form of ZnO nanoparticles, produced using the same procedure, shows a similar size but a denser morphology to that of Fe_3O_4(CA)ZnO (Fig. 5b insert), further confirming that the repulsive effect of the like-charged CA and AC has prevented the deposition of $Zn(Ac)_2$ on the surface of the CA-bound Fe_3O_4. Formation of white coloured ZnO nanoparticles was observed in the reaction mixtures of both hybrid nanoparticles. These particles were separated from the products using an external magnet. The obtained reaction yields were 59.6% for Fe_3O_4(TMAH)-ZnO and 40.6% for Fe_3O_4(CA)-ZnO. The computed mass ratios of Fe_3O_4 to ZnO, based on the ICP-AES analysis result, were 1:4.2 for Fe_3O_4(TMAH)-ZnO and 1:1.6 for Fe_3O_4(CA)-ZnO (Table 1).

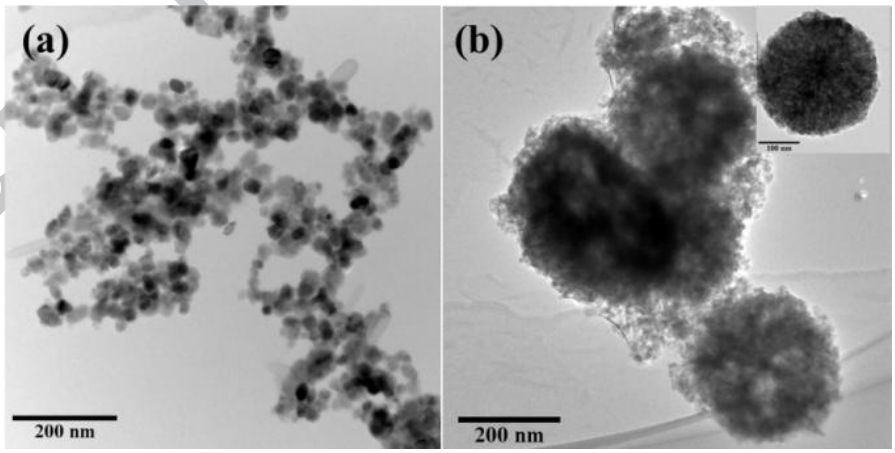

Fig. 5. TEM images of (a) Fe_3O_4(TMAH)-ZnO, (b) Fe_3O_4(CA)-ZnO and (insert) ZnO.

In the FTIR spectra (Fig. 6), the absorption peaks for both Fe-O (530 cm^{-1}) and Zn-O (375 cm^{-1}) stretching vibrations are clearly presented in the produced hybrid nanoparticles. In Fig. 6(a-c), there are two absorption peaks at 1406 cm^{-1} and 1586 cm^{-1}, corresponding to the stretching vibrations of C-O and C=O from acetate groups. These suggest the presence of the

the metal complexes $Zn(OH^{-1})_x(Ac)_{2-x}$ as intermediates during the seed-mediated process. The relative intensities of the two absorption peaks at 540 cm^{-1} and 375 cm^{-1} vary in the FTIR spectra of the Fe_3O_4(TMAH)-ZnO and Fe_3O_4(CA)-ZnO hybrid nanoparticles, further confirming that the ratio of Fe_3O_4/ZnO in these two compounds is different.

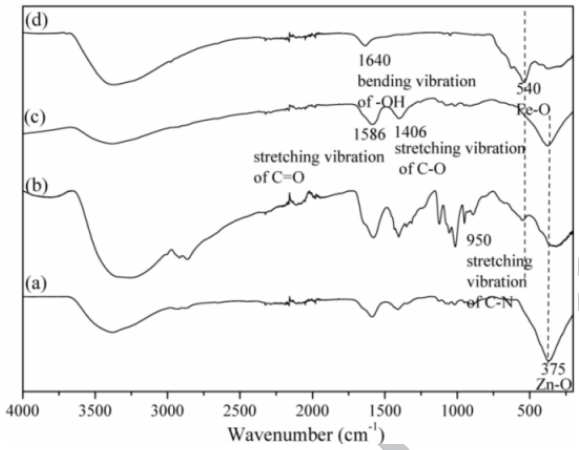

Fig. 6. FTIR spectra of (a) ZnO, (b) Fe_3O_4(TMAH)-ZnO, (c) Fe_3O_4(CA)-ZnO and (d) Fe_3O_4.

The optical properties of the produced nanoparticles were probed by UV-Vis DRS. As presented in Fig. 7, Fe_3O_4 shows a broad absorption peak ranging from 300 nm to 750 nm due to the octahedral ferric ions [25]. An absorption threshold at 391 nm was observed for the ZnO nanoparticles from which the band gap energy was estimated to be 3.2 eV. For TiO_2, the absorption threshold was estimated to be 410 nm and the band gap energy was 3.0 eV. After forming hybrid nanoparticles, a strong absorption was observed below 400 nm. The estimated absorption threshold was 380 nm for Fe_3O_4(TMAH)-ZnO, and 430 nm for Fe_3O_4(CA)-ZnO, indicating a band gap energy of 3.3 eV for the former and 2.9 eV for the latter. Visible light absorption was more dominant in Fe_3O_4(CA)-ZnO, due to the higher Fe_3O_4 content, as previously discussed.

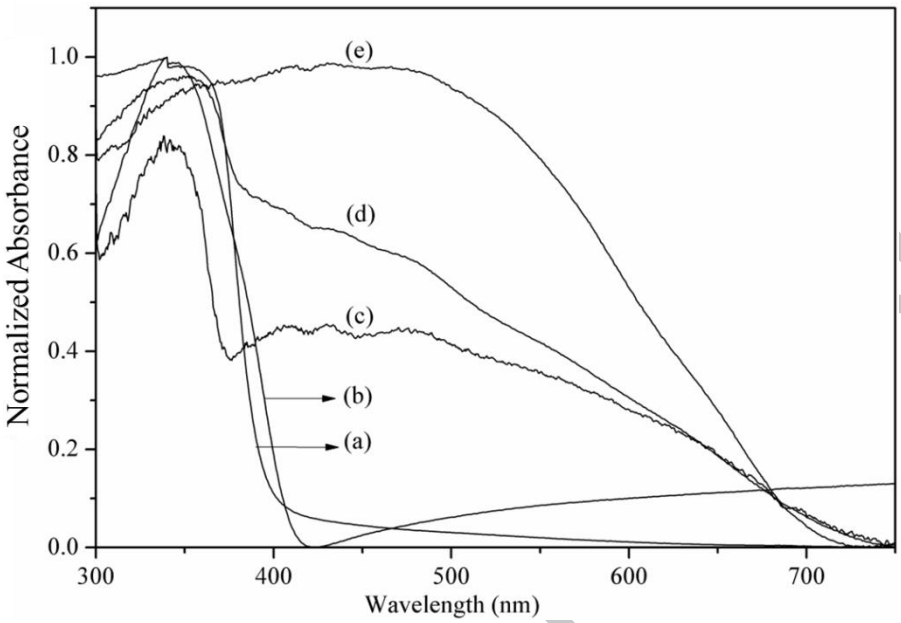

Fig. 7. UV-Vis spectra of (a) ZnO, (b) TiO_2, (c) Fe_3O_4(TMAH)-ZnO, (d) Fe_3O_4(CA)-ZnO and (e) Fe_3O_4.

BET examination showed that both Fe_3O_4(TMAH)-ZnO and Fe_3O_4(CA)-ZnO exhibited type IV isotherms with a type H3 hysteresis loop (Fig. 8a), indicating the mesoporous structure of the hybrid nanoparticles. The calculated pore volumes of Fe_3O_4(TMAH)-ZnO and Fe_3O_4(CA)-ZnO were 0.19 and 0.16 $cm^3\ g^{-1}$, respectively. Using the Barrett-Joyner-Halenda (BJH) model, the estimated pore size of Fe_3O_4(TMAH)-ZnO was approximately 5.8 nm while that of Fe_3O_4(CA)-ZnO was centred at 2 nm. The corresponding surface areas were calculated to be 95.6 $m^2\ g^{-1}$ for Fe_3O_4(TMAH)-ZnO and 73.8 $m^2\ g^{-1}$ for Fe_3O_4(CA)-ZnO. The 29.5% increase in surface area in the Fe_3O_4(TMAH)-ZnO is likely to be due to the smaller particle size. The same examination was carried out on P25. A mean diameter of 24±1 nm was observed, with a measured surface area of 68.9 $m^2\ g^{-1}$, and the pore size was centred at 2.1 nm. The relative pore volume was 0.21 $cm^3\ g^{-1}$, which is slightly greater than that of Fe_3O_4(TMAH)-ZnO (0.19 $cm^3\ g^{-1}$) and much greater than that of Fe_3O_4(CA)-ZnO (0.16 $cm^3\ g^{-1}$).

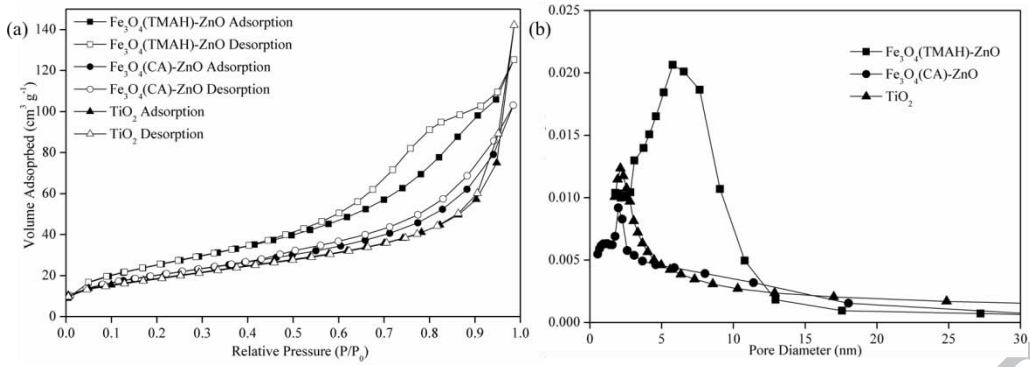

Fig. 8. (a) Nitrogen adsorption-desorption isotherms and (b) BJH pore-size distribution curves for TiO_2, Fe_3O_4(TMAH)-ZnO and Fe_3O_4(CA)-ZnO hybrid nanoparticles.

3.3 Photocatalytic properties of Fe_3O_4-ZnO hybrid nanoparticles

The photodegradation of phenol in the presence of various nanophotocatalysts is displayed in Fig. 9a, in which the initial concentration of phenol was 20 mg L^{-1} and the nanoparticle concentration was 0.325 g L^{-1}. No phenol degradation was observed during the measured time period when Fe_3O_4 was used. After 150 min of irradiation, the percentages of phenol degradation were 71.3% and 54.7% for Fe_3O_4(TMAH)-ZnO and Fe_3O_4(CA)-ZnO, respectively. When ZnO and TiO_2 were used, phenol degradation was 51.8% and 100%, respectively. Based on the data presented in Fig. 9a, the apparent rate constants of these samples were calculated using the previously reported method [13]. The calculated rate constants for TiO_2, Fe_3O_4(TMAH)-ZnO, Fe_3O_4(CA)-ZnO and ZnO were 0.0242, 0.0082, 0.0045 and 0.0039 min^{-1}, respectively (Table 2). An apparent increase in the rate constant was observed for the produced hybrid nanoparticles, in particular for Fe_3O_4(TMAH)-ZnO, when compared with ZnO. This is due to the reduced rate of recombination of photoinduced charge carriers that is well reflected in the photoluminescence (PL) spectra [26] illustrated in Fig. 9b, in which the photoemission intensity of Fe_3O_4(TMAH)-ZnO is much lower than that of ZnO. As discussed in a previous study [9, 27], the photoinduced electrons in the hybrid nanoparticles of Fe_3O_4-ZnO can be transferred from the conduction band of ZnO to the dissolved Fe^{3+} ions, forming Fe^{2+} ions. The formed Fe^{2+} ions then can be oxidized by oxygen in the reaction solution to produce Fe^{3+} ions and release the superoxide radicals. Through such a pathway, the recombination of the photoinduced charge carriers from ZnO is retarded. The presence of elemental iron in the photocatalytic reaction mixture, measured by the ICP-AES, was 0.13 mg L^{-1} (Table 2). This further confirms the hypothesis.

In addition, the Fe_3O_4(TMAH)-ZnO hybrid nanoparticles exhibited better photocatalytic activity than the Fe_3O_4(CA)-ZnO hybrid nanoparticles. As discussed in the previous section, the major differences between these two types of hybrid particle include the particle size, the ZnO content, the structure/morphology and the iron ion concentration in the phenol degradation solution. Firstly, the average size of Fe_3O_4(CA)-ZnO nanoparticles (293±32 nm) is almost nine times bigger than that of Fe_3O_4(TMAH)-ZnO nanoparticles (34.5±6.2 nm), as displayed in Fig. 5. This has resulted in a 29.5% increase in the total surface area of Fe_3O_4(TMAH)-ZnO, as demonstrated by the BET analysis (Fig. 8), resulting in the increased photocatalytic activities. Secondly, the measured mass ratio of Fe_3O_4 and ZnO in the hydrate nanoparticles is 1:4.2 for Fe_3O_4(TMAH)-ZnO and 1:1.6 for Fe_3O_4(CA)-ZnO. The much higher ZnO content in the former would have provided many more catalytic sites for phenol degradation. Thirdly, the larger sized Fe_3O_4(CA)-ZnO and the strong interaction between the Fe_3O_4 and CA might have prevented iron ions being leached out from the hybrid nanoparticles, therefore reducing the electron-hole capture capacity of the hybrid nanoparticles. Indeed, the elemental iron concentration in the Fe_3O_4(CA)-ZnO-containing reaction mixture was 0.06 mg L^{-1}, which is half the amount in the Fe_3O_4(THMA)-ZnO-containing reaction mixture (Table 2). A higher photoemission intensity of Fe_3O_4(CA)-ZnO is also well-evidenced (Fig. 9b).

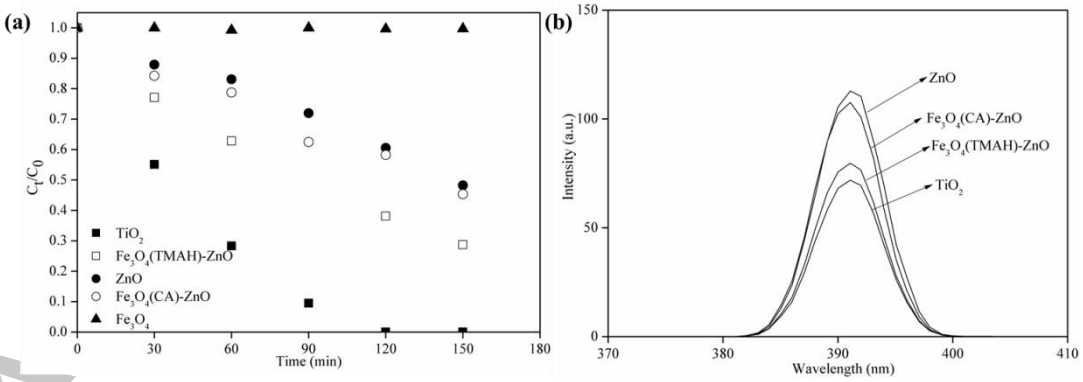

Fig. 9. (a) Phenol concentration changes with time and (b) PL emission spectra of all samples.

In comparison with Fe_3O_4(TMAH)-ZnO, a three times higher phenol degradation rate (0.0242 min^{-1}) was observed when P25 was used, although the photoemission intensities of the two were similar (Fig. 9b). It is worth mentioning that the content of ZnO in Fe_3O_4(TMAH)-ZnO was only 81%, representing a weight concentration of 0.26 g L^{-1} for the active catalyst. When equal amounts of TiO_2 were used, the computed reaction constant became 0.0152 min^{-1}, less than two times that of the rate constant of Fe_3O_4(TMAH)-ZnO.

Considering that, on average, 86% of Fe_3O_4(TMAH)-ZnO nanoparticles can be readily recovered after each photocatalytic reaction, it still is a cost-effective product for photocatalysis.

3.3.1 Optimisation of reaction parameters for Fe_3O_4(TMAH)-ZnO

Reaction parameters, such as catalyst dosage, initial phenol concentration and pH values, exert great influences on the photocatalytic reaction. In this study, when the concentration of Fe_3O_4(TMAH)-ZnO nanoparticles was increased from 0.1 to 0.325 g L^{-1}, increases in both the percentage degradation and the kinetic rate constant were observed due to the increased number of catalyst sites on the catalyst surfaces. However, when the catalyst concentration was further increased, a reduction in the kinetic reaction constant was observed (Table 2 and Fig. 10a). This could be due to the increased particle aggregation at a higher concentration that decreased the surface area and, subsequently, the total number of catalytic sites on the catalyst surfaces. The effect of shielding from the light by the high concentration of catalysts also has been reported [28, 29].

Using Fe_3O_4(TMAH)-ZnO at its optimal concentration of 0.325 g L^{-1}, the effect of initial phenol concentration on the percentage degradation also was investigated. The results are presented in Fig. 10b. A relatively high percentage degradation (78.0%) was observed at 10 mg L^{-1}. There was no significant change when the phenol concentration was increased to 20 mg L^{-1}. However, when the concentration was at 80 mg L^{-1}, the percentage phenol degradation was only 25.9%, indicating that insufficient catalytic sites were present on the surfaces of the hybrid nanoparticles. The excess reaction intermediates formed during the photochemical reaction may also have occupied the active sites, leading to a decrease in degradation rate [30]. The phenol concentration was fixed at 20 mg L^{-1} for other investigations.

A significant effect of pH value, on both phenol degradation percentage and the reaction rate constant, was observed (Fig. 10c). For the photocatalysis of 20 mg L^{-1} phenol using 0.325 g L^{-1} Fe_3O_4(TMAH)-ZnO, when pH was at 2.5, 4, 5.6, 8 and 10, the percentage phenol degradation was 51.9%, 100%, 71.3%, 30.8% and 14.5%, echoing a degradation rate constant of 0.0050, 0.0170, 0.0082, 0.0030 and 0.0013 min^{-1}, respectively. A thirteen-fold increase was evident when pH value was reduced from 10 to 4. The ICP-AES analysis of the photocatalytic reaction mixtures indicated that the iron content was below the detection limit of 0.01 mg L^{-1} at pH 10, but was 22 mg L^{-1} at pH 4. This further demonstrates that the presence of iron ions

can improve the photocatalytic activity by decelerating the fast recombination of photogenerated electron-hole pairs. However, when the pH value was reduced to 2.5, the degradation rate constant was drastically reduced to 0.0050 min^{-1}, although similar amounts of iron ions were detected in the reaction mixture (Table 2). The ICP-AES analysis found a high zinc ion concentration, 220 mg L^{-1}, in the reaction mixture, indicating a high dissolution of the catalytic zinc oxide. When the pH value of the reaction mixture was increased to 8 and 10, the phenol degradation rate became much slower (Table 2 and Fig. 10c). This can be attributed to the low concentration of iron ions present in the phenol solution, which was undetectable by ICP-AES (Table 2). In addition, the basic solution could lower the oxidation potential of hydroxyl radicals, leading to a decrease in oxidation efficiency of the phenol in solution [31, 32].

Similar investigations also were performed on Fe_3O_4(CA)-ZnO. The reaction parameters, the percentages of phenol removal and the rate constants are summarised in Table 2. Although the effects of these parameters on the phenol degradation are similar to those of the Fe_3O_4(TMAH)-ZnO, the photoreactivity of Fe_3O_4(CA)-ZnO is generally poorer than that of Fe_3O_4(TMAH)-ZnO in all cases.

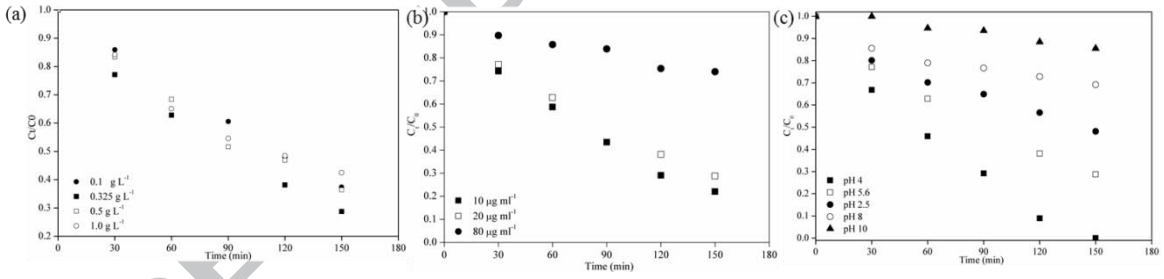

Fig. 10. Phenol degradation by Fe_3O_4(TMAH)-ZnO at various (a) catalyst concentrations, (b) phenol concentrations and (c) pH values.

3.4 Comparison of photocatalytic properties of different nanoparticles

The photocatalytic properties of Fe_3O_4(TMAH)-ZnO, Fe_3O_4(CA)-ZnO and P25 are summarised and presented in Fig. 11. For Fe_3O_4(TMAH)-ZnO, an optimal degradation rate constant of 0.0170 min^{-1} was achieved at pH=4, at which pH value the degradation constant is 0.0085 min^{-1} for Fe_3O_4(CA)-ZnO and 0.0020 min^{-1} for P25. In contrast to these observations, P25 performed its best at pH=5.6, presenting a rate constant of 0.0242 min^{-1}, in comparison with 0.0082 min^{-1} and 0.0045 min^{-1} for Fe_3O_4(TMAH)-ZnO and Fe_3O_4(CA)-ZnO, respectively. However, when the amount of TiO_2 was reduced to 0.26 g L^{-1}, which is equivalent to the

active ingredient of ZnO, the rate constant of TiO_2 reduced to 0.0154 min^{-1}, which is slightly lower than that of Fe_3O_4(TMAH)-ZnO at pH=4. At pH=10, the three types of nanoparticles showed similar catalytic reactivities towards phenol degradation.

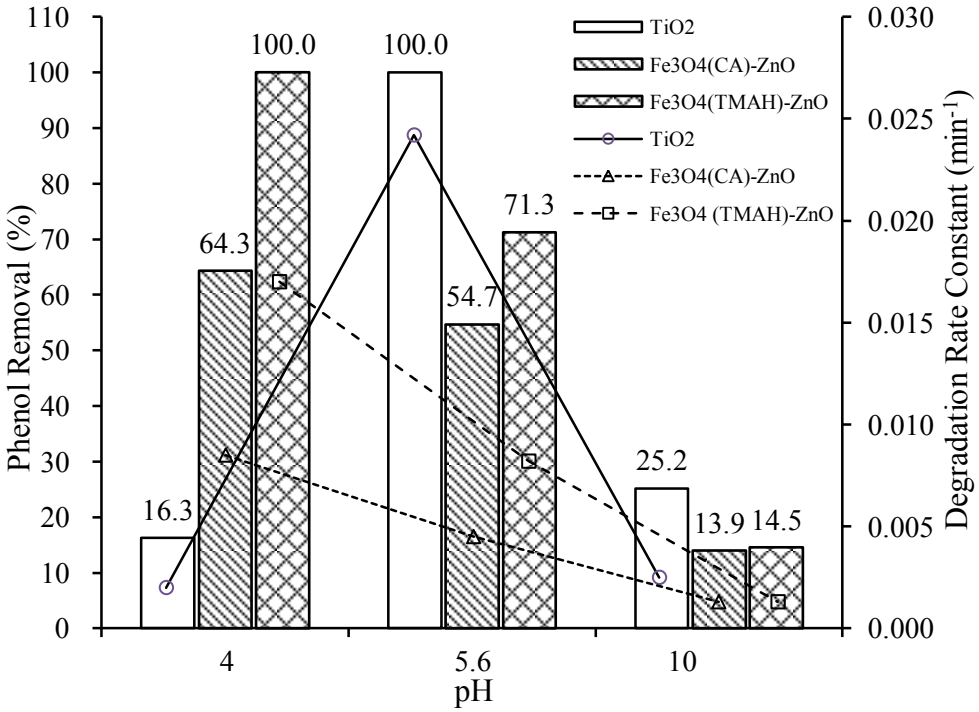

Fig.11. Percentage phenol degradation under various pH conditions. The catalyst concentration was 0.325 g L^{-1}. The initial phenol concentration was 20 mg L^{-1}.

4 Conclusion

In summary, magnetite (Fe_3O_4) nanoparticles were bound with a cationic surfactant (TMAH) and an anionic surfactant (CA), and then used as seeding templates to produce Fe_3O_4-ZnO hybrid nanophotocatalysts. Both surfactants have shown the ability to stabilise the Fe_3O_4 nanoparticles, which is believed to be due to the presence of charged tetramethylammonium ions and carboxyl ions on the nanoparticles. However, the hybrid nanoparticles produced from different stabilisation methods exhibited very different photocatalytic properties towards phenol degradation. The TMAH-bound nanoparticles, Fe_3O_4(TMAH)-ZnO, have shown an excellent rate constant (0.0170, pH=4) for phenol degradation and a high recoverability for reuse (86%). They outperformed P25 under acidic conditions and were comparable to TiO_2 under less acidic or more alkaline conditions (Fig.11). The stronger photocatalytic performance, the smaller particle size and the denser, more uniform structure of Fe_3O_4(TMAH)-ZnO, in comparison with those qualities of the CA-bound hybrid nanoparticles (Fe_3O_4(CA)-ZnO), demonstrated that the TMAH is more

favourable than CA as the surfactant when Fe_3O_4 is used to produce magnetite-supported heterogeneous catalysts, especially when the deposited catalytic species are negatively charged. The results also indicated that the overall performance of the hybrid nanophotocatalyst is dependent upon the reaction conditions. For the investigated phenol degradation, 10-20 mg L^{-1} phenol, 0.325 g L^{-1} photocatalyst and an acidic environment of pH=4 to pH=5.6 are optimal. Dissolution of both Fe_3O_4 and ZnO was observed during the photocatalysis. While the dissolution of zinc may have led to the reduced photocatalytic activities, the presence of the dissolved iron ions was found to be beneficial to the phenol degradation, which supports the speculation that the iron ions acted as photoexcited electron-trappers to prevent the fast recombination of the charge carriers. We trust that the produced Fe_3O_4(TMAH)-ZnO hybrid nanoparticles are of great potential for the cost-effective removal of phenol and other organic contaminants. We also are investigating the potential applications of the hybrid nanoparticles in effective photodynamic cancer therapies [15, 16].

References

1. Polshettiwar, V., et al., *Magnetically recoverable nanocatalysts.* Chem. Rev., 2011. **111**: p. 3036-3075.
2. Gawande, M.B., P.S. Branco, and R.S. Varma, *Nano-magnetite (Fe_3O_4) as a support for recyclable catalysts in the development of sustainable methodologies.* Chem. Soc. Rev., 2013. **42**: p. 3371-3393.
3. Mahmoudi, M., A. Simchi, and M. Imani, *Cytotoxicity of uncoated and polyvinyl alcohol coated superparamagnetic iron oxide nanoparticles.* J. Phys. Chem. C, 2009. **22**: p. 9573-9580.
4. Liu, S.Q., *Magnetic semiconductor nano-photocatalysts for the degradation of organic pollutants.* Environ. Chem. Lett., 2012. **10**(3): p. 209-216.
5. Ambashta, R.D. and M. Sillanpää, *Water purification using magnetic assistance: A review.* J. Hazard. Mater., 2010. **180**(1–3): p. 38-49.
6. Zhou, M., J. Yu, and B. Cheng, *Effects of Fe-doping on the photocatalytic activity of mesoporous TiO_2 powders prepared by an ultrasonic method.* J. Hazard. Mater., 2006. **137**(3): p. 1838-1847.
7. Karunakaran, C., P. Vinayagamoorthy, and J. Jayabharathi, *Nonquenching of Charge Carriers by Fe3O4 Core in Fe3O4/ZnO Nanosheet Photocatalyst.* Langmuir, 2014. **30**(49): p. 15031-15039.
8. Singh, S., K.C. Barick, and D. Bahadur, *Fe3O4 embedded ZnO nanocomposites for the removal of toxic metal ions, organic dyes and bacterial pathogens.* Journal of Materials Chemistry A, 2013. **1**(10): p. 3325-3333.
9. Feng, X., et al., *High performance,recoverable Fe_3O_4-ZnO nanoparticles for enhanced phtocatalytic degradation of phenol.* Chem. Eng. J., 2014. **244**: p. 327-334.
10. Hamley, I.W., *Nanotechnology with soft materials.* Angew. Chem. Int. Edit., 2003. **42**(15): p. 1692-1712.
11. Sahoo, Y., et al., *Aqueous ferrofluid of magnetite nanoparticles: Fluorescence labeling and magnetophoretic control.* J. Phys. Chem. B, 2005. **109**(9): p. 3879-3885.
12. Sousa, M.H., F.A. Tourinho, and J. Depeyrot, *New electric double-layered magnetic fluids based on copper, nickel, and zinc ferrite nanostrucures.* J. Phys. Chem. B, 2001. **105**: p. 1168-1175.
13. Lesnikovich, A.I., et al., *Dispersity of magnetite in magnetic liquids and the interaction with a surfactant.* J. Magn. Magn. Mater., 1990. **85**(1-3): p. 14-16.
14. Sun, Y., et al., *An improved way to prepare superparamagnetic magntite-silica core-shell nanoparticles for possible biological application.* J. Magn. Magn. Mater., 2005. **285**(1-2): p. 65-70.
15. Feng, X., S. Zhang, and X. Lou, *Controlling silica coating thickness on TiO_2 nanoparticles for effective photodynamic therapy.* Colloid Surface B, 2013. **107**: p. 220-226.
16. Feng, X., et al., *A novel folic acid-conjugated TiO_2–SiO_2 photosensitizer for cancer targeting in photodynamic therapy.* Colloid Surface B 2015. **125**: p. 197-205.
17. Panias, D., et al., *Mechanisms of dissolution of iron oxides in aqueous oxalic acid solutions.* Hydrometallurgy, 1996. **42**: p. 257-265.
18. Racuciu, M., *Synthesis protocol influence on aqueous magnetic fluid properties.* Curr. Appl. Phys., 2009. **9**: p. 1062-1066.
19. Liu, X., et al., *Preparation and characterization of amino-silane modified superparamagnetic silica nanospheres.* J. Magn. Magn. Mater., 2004. **270**(1-2): p. 1-6.

20. Sousa, M.E., et al., *Stability and relaxation mechanisms of citric acid coated magnetite nanoparticles for magnetic hyperthermia.* J. Phys. Chem. C, 2013. **117**: p. 5436-5445.
21. Kalska-Szostko, B., et al., *Stability of core-shell magnetite nanoparticles.* Colloids Surf., B, 2014. **113**: p. 295-301.
22. Todorovsky, D.S., et al., *Preparation and charaterization of yttrium-iron citric acid complexes.* Croat. Chem. Acta, 2002. **75**(1): p. 155-164.
23. Cheng, F., et al., *Charaterization of aqueous dispersions of Fe_3O_4 nanoparticles and their biomedical applications.* Biomaterials, 2005. **26**(7): p. 729-738.
24. Sahoo, Y., et al., *Aqueous ferofluid of magnetite nanoparticles: Flurorescence labeling and magnetophoretic control.* J. Phys. Chem. B, 2005. **109**: p. 3879-3885.
25. Xing, S., et al., *Characterization and reactivity of $Fe_3O_4/FeMnO_x$ core/shell nanoparticles for methylene blue discoloration with H_2O_2.* Appl. Catal., B, 2011. **107**(3–4): p. 386-392.
26. Wang, Y., et al., *Controllable synthesis of ZnO nanoflowers and their morphology-dependent photocatalytic activities.* Sep. Purif. Technol., 2008. **62**(3): p. 727-732.
27. Tung, W.S. and W.A. Daoud, *New approach toward nanosized ferrous ferric oxide and Fe_3O_4-doped titanium dioxide photocatalysts.* ACS Appl. Mater. Interfaces, 2009. **1**: p. 2453–2461.
28. Chen, D. and A.K. Ray, *Photodegradation kinetics of 4-nitrophenol in TiO_2 suspension.* Water Res., 1998. **32**(11): p. 3223-3234.
29. Wang, Y., et al., *Synthesis and photo-catalytic degradation property of nanostructured-ZnO with different morphology.* Mater. Lett., 2008. **62**(15): p. 2359-2362.
30. Wei, T.Y. and C.C. Wan, *Heterogeneous photocatalytic oxidation of phenol with titanium dioxide powders.* Ind. Eng. Chem. Res., 1991. **30**(6): p. 1293-1300.
31. Hayat, K., et al., *Effect of operational key parameters on phtocatalytic degradation of phenol using nano nickel oxide sysnthesize by sol-gel method.* J. Mol. Catal. A: Chem., 2011. **336**: p. 64-71.
32. Chiou, C.H., C.Y. Wu, and R.S. Juang, *Influence of Operating Parameters on Photocatalytic Degradation of Phenol in UV/TiO_2 Process.* Chem. Eng. J., 2008. **139**: p. 322-329.

Graphical abstract

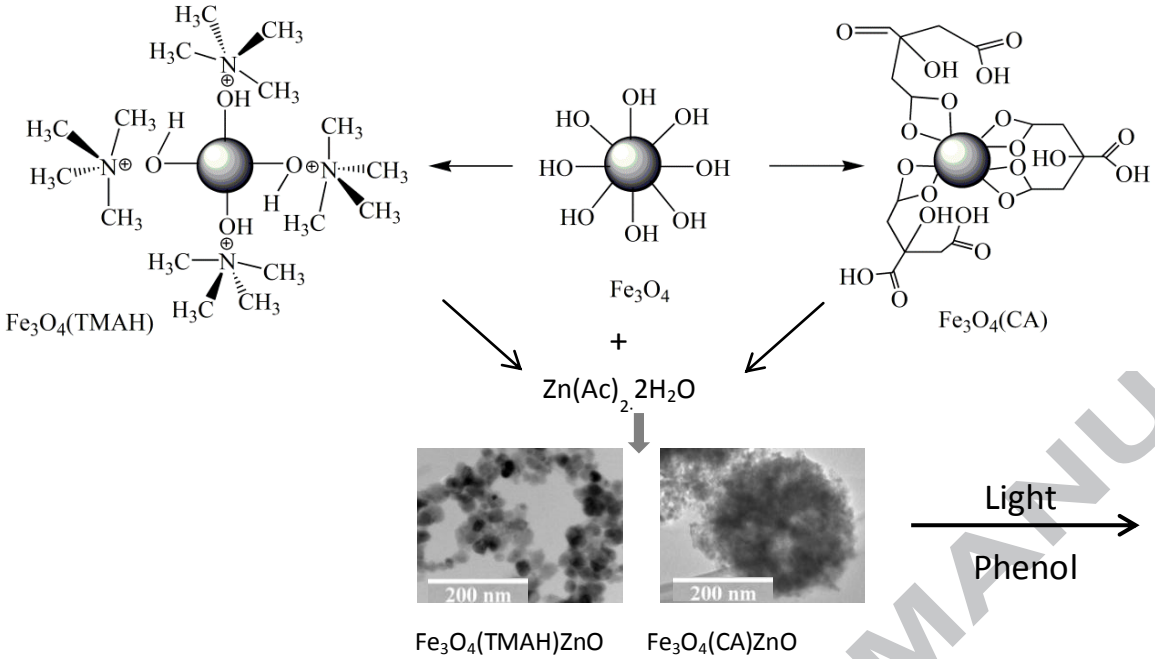

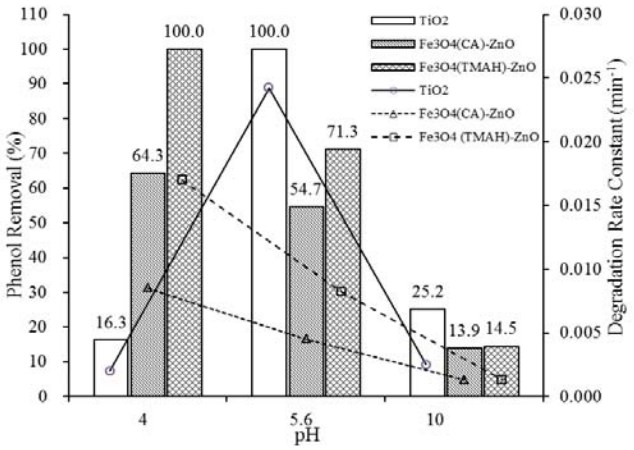

Highlights

- Highly reactive and recoverable Fe_3O_4-ZnO-based photocatalysts are synthesized
- Binding TMAH onto the surface of Fe_3O_4 dramatically improves the catalytic property
- Binding CA onto the surface of Fe_3O_4 reduces the effective deposition of active ZnO
- Altering pH values significantly changes the photocatalytic activities of Fe_3O_4-ZnO